Additive Manufacturing 81 (2024) 104001

Contents lists available at ScienceDirect

Additive Manufacturing

journal homepage: www.elsevier.com/locate/addma

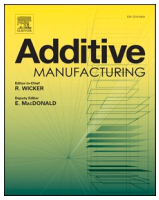

In-situ interferometric curing monitoring for digital light processing based vat photopolymerization additive manufacturing

Yue Zhang, Haolin Zhang, Xiayun Zhao *

ZXY Intelligent Precision Advanced Manufacturing (ZIP-AM) Laboratory, Department of Mechanical Engineering & Materials Science, University of Pittsburgh, Pittsburgh, PA 15261, USA

ARTICLE INFO

Keywords:
Additive manufacturing
Photopolymerization
Degree of curing
In-situ monitoring
Interferometry

ABSTRACT

Digital light processing (DLP) based vat photopolymerization (VPP) is an additive manufacturing (AM) technology that projects sequential optical masks to selectively cure cross-sectional patterns layer by layer. DLP-VPP is widely used in rapid prototyping and fabrication of diverse products ranging from consumer goods to soft robotics. Degree of curing (DoC) is one primary performance metric for photopolymer-based AM processes due to its high correlation with key material properties such as density and elastic modulus. Yet there is a lack of in-situ monitoring approaches to understand and control the photopolymerization process and part properties. State-of-the-art works use in-situ Fourier-transform Infrared Spectroscopy (FT-IR) and atomic force microscopy, which would interfere with the process and material and can only measure DoC at one single point each time. This work aims to develop a cost-effective, non-interruptive, non-invasive, and full-field in-situ interferometric curing monitoring (ICM) method for revealing the spatiotemporally resolved curing dynamics and material evolution during DLP-VPP. To this end, a physics-based sensor model is derived, and machine learning-aided sensor data processing and analytics methods are developed to address the unique measurement challenges in DLP-VPP-specific ICM. Using the developed ICM model and methods, the acquired interferogram data is cleaned, classified, and calculated for estimating each voxel's refractive index, which is an indicator of optical density as well as physical density. Then, a DoC prediction model is created by correlating the in-situ ICM-measured refractive index to ex-situ FT-IR-measured DoC. Our experiment results demonstrate that the developed ICM system and methods are capable of measuring the geometry (e.g., lateral dimensions and shapes) of printed part as well as capturing the changes in curing speed, refractive index, and DoC due to the different exposure masks and intensities being used in DLP-VPP. It has the potential to provide real-time multi-modality measurement and enable closed-loop feedback control for enhancing the DLP-VPP process reproducibility and print quality.

1. Introduction

1.1. Vat photopolymerization (VPP) and need for advanced process monitoring

Additive Manufacturing (AM) could fabricate objects with reduced material waste and higher efficiency compared to traditional manufacturing methods. Due to its high resolution and rapid production speed, vat photopolymerization (VPP) is one of the most commonly used AM technologies and widely applied to manufacture a variety of products like flexible electronics, tissues and scaffolds [1,2]. VPP processes typically print layer by layer as in stereolithography (SLA) and digital light processing (DLP). It can also create items in a layer-less approach by continuous moving the print head such as continuous liquid interface production (CLIP) and computed axial lithography (CAL) [3,4]. The CAL is a volumetric VPP process, which shines varying light patterns into a rotating volume of resin. It can print large volume objects with higher speed and accuracy compared to layer-based VPP AM. Various monitoring methods are applied to understand the process dynamics and part properties during these different VPP processes. For example, Li et al. applies a color Schlieren imaging system to reconstruct the gradient of refractive index of the CAL process [5]. Their in-situ refractive index monitoring system enables a construction of spatial and temporal gradient of refractive index, but the measurement range and accuracy are limited by non-uniform background hue and nonlinear hue-deflection relationship. The Schlieren-based system has also been

* Corresponding author.
E-mail address: xiayun.zhao@pitt.edu (X. Zhao).

https://doi.org/10.1016/j.addma.2024.104001
Received 21 November 2023; Received in revised form 4 January 2024; Accepted 23 January 2024
Available online 1 February 2024

used in a SLA process to study the in-situ voxel growth dynamics [6]. In particular, this Schlieren system is modified with two levels of magnification to allow focusing on small areas (i.e. single voxel), while other methods like total internal reflection (TIR)-based refractive index measurement only measure the whole area [7]. However, the Schlieren method requires complex optical system that makes it difficult to be implemented on VPP printers and can only captures the side view of a printed part. Higgins et al. implements an atomic force microscopy (AFM) to a DLP process to measure the mechanical properties during polymerization process, but the cantilever tip needs to touch the liquid resin and the cured part [8]. Fourier-transform Infrared Spectroscopy (FT-IR) is also employed to estimate the conversion of relevant functional groups by monitoring the reduction of corresponding absorption peaks but only measures a single point [9,10]. Raman microscopy is capable of measuring the conversion of functional groups at different points through point, line or area scan, facing challenges in directing curing light to the sample under microscopy. Moreover, the scan is time consuming [11]. All of these state-of-the-art VPP process monitoring methods would interfere with the complete part formation [10,12,13]. Besides, they often come with limitations including high cost, limited view, destructiveness, and operation complexity on VPP printers. Overall, there is a lack of cost-efficient, non-destructive and easily implementable in-situ monitoring methods for characterizing curing kinetics and part properties during VPP processes.

1.2. Interferometric monitoring for VPP processes

1.2.1. Existing works

The interferometry technique is a non-destructive and reliable method that has been demonstrated for being able to measure physical and chemical properties, such as refractive index and thickness of the cured part during photopolymerization processes for monitoring [14–16]. In [14], a low coherence interferometry is applied to simultaneously monitor the volume shrinkage and refractive index evolution during a photopolymerization process with dental materials [14]. In their research, the reliability of the interferometry technique is validated by comparing its results to refractive index measurements obtained from a conventional refractive index characterization device, namely the Abbé refractometer. Some other researchers used a double-interferometer to monitor the refractive index and sample thickness by measuring the phase shift of light passing through the sample cell of photopolymer [17]. Zhao et al. developed an interferometric curing monitoring and measurement (ICM&M) method to monitor the cured height during a simplified DLP process named as exposure-controlled projection lithography (ECPL) by developing a multi-beam interference model and sensor data analytics method for estimating and integrating instantaneous frequency values [18–22]. Their method involves a refractive index calibration procedure to ensure accuracy and an online evolutionary parameter estimation algorithm to analyze real-time data acquired from the interferometric monitoring of ECPL for height measurement.

1.2.2. Novelty of this research on interferometric monitoring of VPP

Despite the existing monitoring capability mentioned above, there exists a notable omission in the oversight of a crucial metric — the Degree of Curing (DoC) in photopolymerization. The DoC is important in comprehending VPP processes as it serves as a reflection of the degree of crosslinking among monomers and significantly affects density and other properties. For example, photocured parts' mechanical properties such as Young's modulus, tensile strength, and hardness can be predicted from DoC based on Yang's studies [23]. Moreover, optical properties such as refractive index of the photocured composites is found to be related with DoC [24]. In [24] the authors prepare resins with different filler loadings and monitor their real-time DoC and refractive index during the photopolymerization process. Their results show that for an unfilled resin (without any fillers), there is a linear relationship between the refractive index and degree of conversion.

The discernible connections between DoC, refractive index, and mechanical properties have motivated our new research, as outlined in this paper. Our focus involves expanding the ICM&M of ECPL for measuring DoC in the context of DLP-VPP. This extension allows for estimating the diverse properties of the printed components with enhanced accuracy and depth.

Distinguishing itself from prior work, this research contributes in two main aspects. First, we advance the interferometric monitoring methodology to accommodate a broader scope, specifically in monitoring a general DPL-VPP process involving a moving build stage. This contrasts with the static stage employed in ECPL, which is a simplified process tailored for certain niche applications. Details on the challenges encountered and the corresponding solutions adopted are introduced in Section 1.3. Secondly, our work addresses a limitation in the previously reported ICM&M method, which solely outputs the cured height of printed samples for a specific DLP process (i.e., ECPL) that prints relatively simple geometries on a stationary build platform. In this research, we broaden the scope to measure not only geometrical dimensions but also curing dynamics, specifically focusing on the DoC.

In summary, this work significantly contributes by establishing a universal ICM method applicable to common and complex DLP-based VPP (DLP-VPP) processes, such as CLIP, capable of printing real 3D parts with a moving build stage. By incorporating the developed ICM method into the DLP-VPP process, a comprehensive understanding of the complex process dynamics and material's curing behavior as well as the ability to predict mechanical properties can be achieved, contributing to DLP-VPP process optimization and control for printing high-quality 3D parts.

1.3. Overview of this work

The primary goal of this work is to formulate and demonstrate a methodological framework for an in-situ interferometric curing monitoring (ICM) system and method. This framework is designed to encompass not only geometry measurement but also the in-process measurement of the refractive index and prediction of the DoC for printed parts. This comprehensive approach is tailored specifically for a standard DLP-based 3D printing VPP process.

Specifically, the DLP-VPP process monitoring via ICM faces the following challenges that will be addressed in this work. During the DLP-VPP process, light is illuminated from the bottom of resin chamber, after one layer of resin is cured on the print head, the stage with the print head where the printed part is attached will move up and another layer of resin will be cured beneath the previous cured layer. Therefore, the ICM sensor model needs to be modified. Moreover, the stage movement and resin flow tend to induce more noise in the interferogram images, necessitating a machine leaning aided sensor data processing method to detect good pixels with higher signal-to-noise ratio (SNR). Machine learning based classification method has been widely used in outlier or defect detections in various fields including manufacturing, healthcare, and financial services [25,26]. One specific signal input for machine learning model is the time signal. Pragmatically, different machine learning models targeting to process time signals are proposed to solve a range of well-defined problems such as signal classification, signal filtering, and signal forecasting. For example, the one-dimensional convolutional neural network (CNN) is applied to classify Electroglottography (EGG) signal to help health care services [27]. Regarding the additive manufacturing industry, machine learning models are used to process time signals such as acoustic signals for defect detection for laser powder bed fusion (LPBF) process. For VPP processes, machine learning methods are usually applied for optimization of material parameters like resin formulation and processing parameters like grayscale values of light masks [28,29]. In this work, the machine learning model is designed as the signal classification tool to reduce the effects of noise in the in-situ monitoring process. The developed machine learning

model overall enhances the accuracy of the monitoring system.

The remainder of the paper is as follows, Section 2 discusses the VPP and ICM experimental setups, materials, and experiment design. Section 3 demonstrates the ICM method, followed by the results and discussion in Section 4. The conclusion and future work are presented in Section 5.

2. Experiment systems

2.1. DLP-VPP and ICM systems

The experimental setup of DLP-VPP system is shown in Fig. 1(a). The DLP-VPP printer includes one commercial DLP projector (PRO4500, Wintech Digital, Carlsbard, CA) with Ultraviolet(UV) light LED source that has a wavelength of 365 nm. In this work, UV light is used as the curing light according to the absorbance spectrum of used initiator. For a clear interference pattern, a glass slide is used as the printer head in this work, which is taped on a linear travel motorized stage (LTS-150, Thorlabs, Newton, NJ).

Our ICM system (as shown in Fig. 1) comprises the following components: (1) a collimated green laser of wavelength of 532 nm (CPS532, Thorlabs, Newton, New Jersey); (2) a beam expander (GBE10-A, Thorlabs, Newton, New Jersey); (3) a 50:50 (R:T) Split Ratio beam splitter (BS013, Thorlabs, Newton, New Jersey); and (4) a CMOS camera (acA2040–120 μm, Basler, Exton, PA) with a sampling frequency of 120 Hz. The optics and camera are fixed above the moving print stage by a 3D printed fixture. With the designed ICM system, interference patterns caused by the optical path difference through a growing part during the DLP-VPP process can be captured by the camera and recorded into an interferogram video. To obtain optimum interferograms, different substrate materials are tried. Compared to Polydimethylsiloxane (PDMS) and Teflon FEP films, quartz glass slides can create better interference patterns due to its smooth surface, higher refractive index, and rigidity. The smoother surface and more uniform thickness of the quartz glass slide can reduce surface irregularities, thereby promoting normal incidence. Also importantly, the higher refractive index of quartz glass can increase surface reflectivity. In addition, unlike elastic PDMS and Teflon films, which tend to deform and bend when resin is added, quartz glass slides can maintain flatness

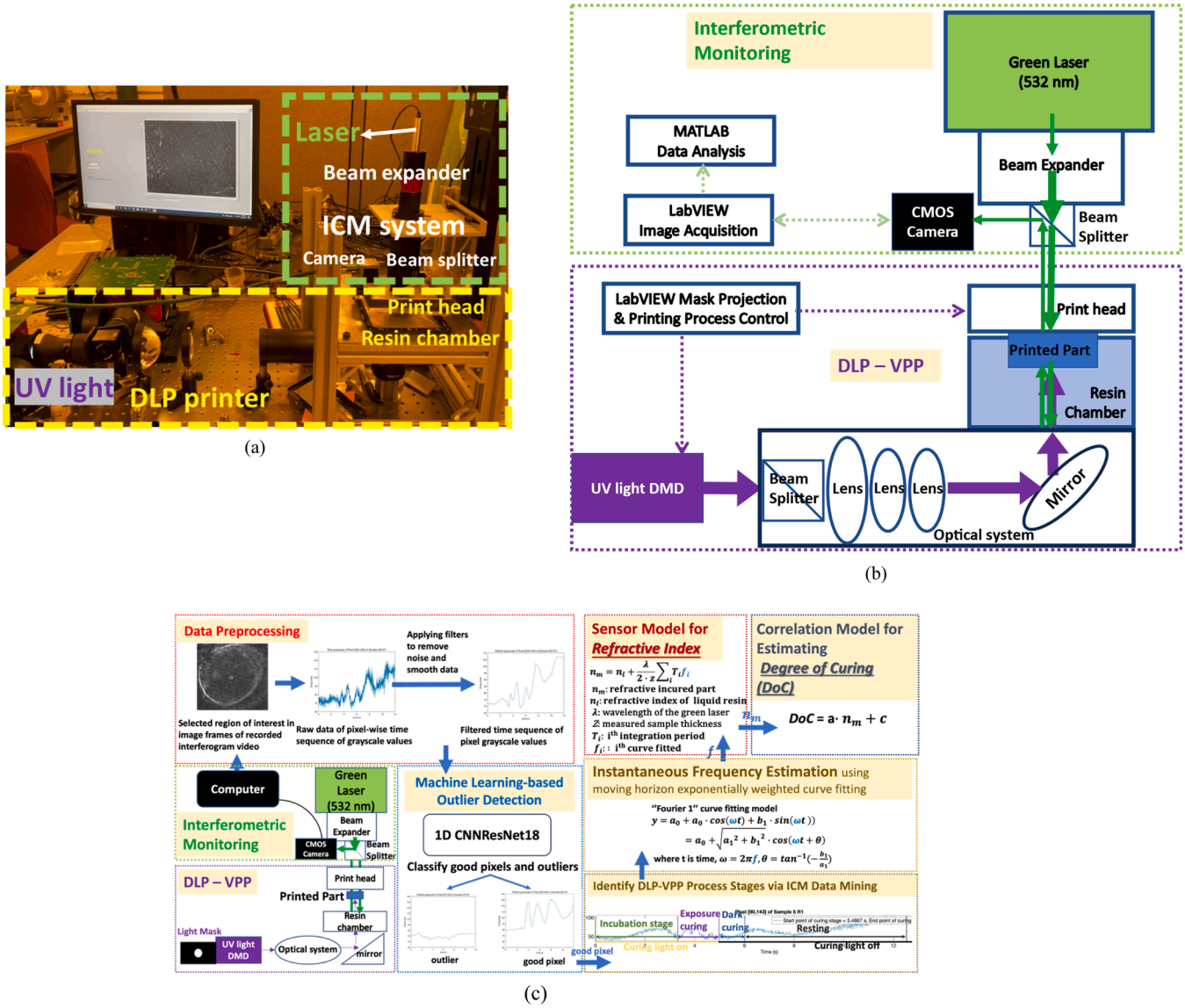

Fig. 1. Overview of the developed DLP-ICM system and methods. (a) Experiment setup. (b) Schematic of the optical layout. (c) Methodological framework of in-situ interferometric monitoring for DLP-VPP process. (d) Measurement flowchart to clarify the workflow in (c). (e) An example of the ICM data: time series of grayscale value of a representative pixel in one sample from Experiment Set 4 and its corresponding instantaneous frequency estimated by the methods as introduced in Section 2.2.

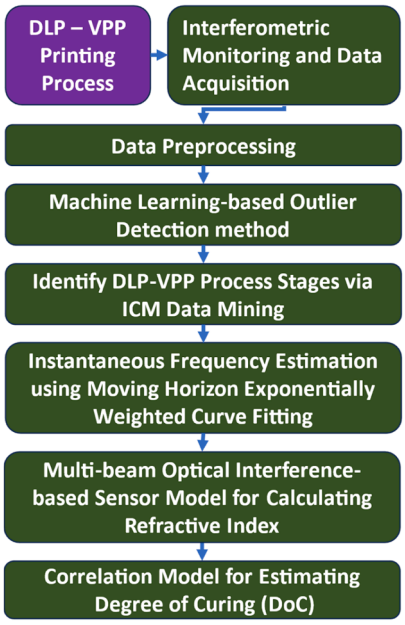

(d)

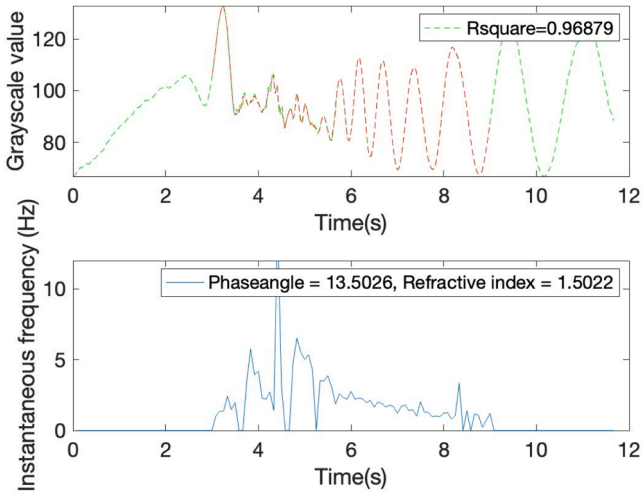

(e)

Fig. 1. (*continued*).

and create accurate and consistent interference patterns. All these favorable attributes of quartz glass greatly help enable the formation of clear and distinct interference fringes and enhance the imaging of resulting interferograms. Meanwhile, it is worth pointing out that quartz glass is also desired as the resin substrate to allow for a good transmission of UV light masks into the resin. Therefore, quartz glass is recommended to be used as the resin chamber substrate to facilitate the ICM of DLP-VPP. Overall, Fig. 1 presents the experimental setup, optical layout, framework of data acquisition and analysis, measurement flowchart, and exemplary data for illustrating the developed DLP-specific ICM (DLP-ICM) system and methods.

2.2. Overview of the developed methodological framework of DLP-ICM

The overall DLP-ICM workflow is as follows.

(1) Implement the ICM system (Section 2.1) in situ to record an interferogram video during a DLP-VPP process.
(2) Characterize the refractive index of the precursor liquid resin that is needed to solve the ICM sensor model (elaborated in Section 3.1).
(3) Extract pixel-wise time series of image grayscale values from the sequential interferogram frames in the acquired ICM video. Preprocess all pixels' time series of grayscale value with filters and implement machine learning on the filtered dataset to detect good pixels that exhibit distinct signals reflecting the DLP-VPP process characteristics (elaborated in Section 3.2).
(4) Analyze each good pixel's data (i.e., filtered time sequence of grayscale in Step (3)) to identify the characteristic stages of a DLP-VPP process (elaborated in Section 3.3).
(5) Apply adaptive Fourier curve fitting (elaborated in Section 3.4) to the curing stage data identified in Step (4) to estimate all the instantaneous frequency values through a DLP-VPP process, as shown in Fig. 1(c).
(6) Plug the refractive index of liquid resin from Step (2) and the estimated instantaneous frequency values from Step (5) into the

ICM sensor model (see Section 3.1) to calculate the desired refractive index of VPP printed parts. In theory a 2-dimensional map of refractive index across the printed part can be obtained by analyzing all pixels' time series of grayscales using the methods above excluding the machine learning aided good pixels detection procedure. In practice, however, for efficiency and accuracy only these good pixels identified in Step (3) need to be analyzed yielding meaningful measurement result, especially given noisy monitoring data.

(7) Develop a correlation model between refractive index and DoC using the average of the ICM-measured refractive index values and the FT-IR measured average DoC. The reason for using average refractive index is that the FT-IR sensor size is typically larger than the ICM camera pixel size and thus cannot measure pixel-wise DoC accurately. In theory, a 2-dimenionsal profile of DoC can be obtained by plugging individual pixel's refractive index value that is measured by ICM to the developed refractive index-DoC correlation model.

(8) Use the developed DLP-ICM method and refractive index-DoC model as introduced above to monitor subsequent DLP-VPP processes and predict the resulting parts' DoC values. The DoC prediction via ICM data analysis can be validated by comparing against FT-IR characterization.

As a summary, Fig. 1(c) shows a schematic overview of the DLP-specific ICM method along with a demonstration of raw ICM data and the corresponding instantaneous frequency estimation result shown in Fig. 1(e). More results will be available in Section 4.

2.3. Materials

The resin used in this work is prepared using trimethylolpropane triacrylate (TMPTA) as monomer and 0.5 wt% 2,2dimethoxy-1,2-diphenylethan-1-one (DMPA, Irgacure-651) as an UV light photo-initiator. This resin recipe is adapted from [18], it is reported that this resin formulation can achieve more than 90% transmission in the visible spectrum after fully cured. All the chemicals are purchased from Sigma-Aldrich. All the materials are used as received without any additional modifications.

3. Method of in-situ interferometric monitoring of DLP-VPP

With the designed ICM system being deployed to monitor a typical DLP-VPP process, one will be able to acquire streaming interferogram images in a video file that provide raw ICM data. This section introduces the methods of processing and analyzing the ICM data to extract relevant DLP-VPP process signatures and measure physical quantities of refractive index that will be used to further infer the DoC.

3.1. ICM sensor modeling

An explicit physics-based sensor model for the DLP-specific ICM system is developed based on multi-beam interference optics as illustrated Fig. 2. Overall, the assumption is that the actual thickness of each layer is the same as the pre-determined process setting of layer thickness. Thus, given a layer thickness known from the process setting and an optical path length measured by the interferometry, one can estimate the effective refractive index of each layer, which depends on the polymerization process especially the degree of cure.

As Fig. 2 shows, after a coherent light beam from the ICM system is projected upon the print head, it will go through the print head, printed part, liquid resin, and resin substrate. The light beam will reflect from and transmit through each interface during the propagation. At the end, these multiple reflected optical wave beams overlap above the print head and form an interference field, which is captured by the ICM camera as an interferogram image. Mathematically, the addition of the

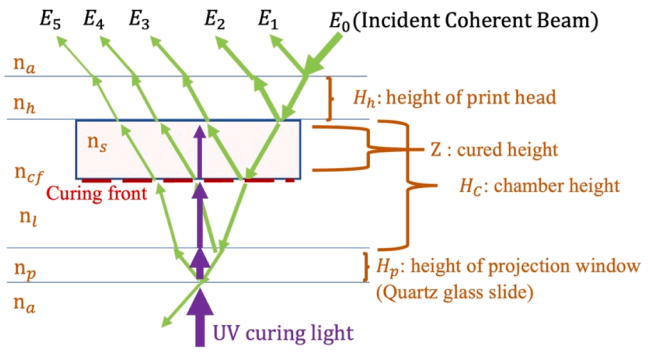

Fig. 2. Schematic illustration of our DLP-specific ICM sensor modeling based on multi-beam interference optics. $n_a, n_p, n_l, n_{cf}, n_s, n_h$ are refractive index of air, projection window, liquid resin, curing front, cured solid part, and print head, respectively. This model is adapted from [20] to incorporate the DLP-VPP process setup. Note that the propagation of beam is shown with an angle that is exaggerated for clarification purpose. In theory normal incidence should be used to ensure accurate measurement. In practice a good vertical alignment of ICM camera and optics with DLP light axis and print head is required.

vectors of the light wave components as shown in Eq. (1), results the total wave represented in Eq. (2) [20].

$$E_n = A_n e^{i\phi_n}, n = 1, 2, \ldots, 5 \tag{1}$$

where A_n is the real positive amplitude, and $\varnothing_n$ is the phase angle of each wave.

$$E_T = \sum_{n=1}^{5} E_n = \sum_{n=1}^{5} A_n e^{i\phi_n} \tag{2}$$

When the field is observed by a CMOS camera, the irradiance, I can be measured [16]. I is proportional to the squared module of the amplitude of the field, as shown in Eq. (3).

$$I = |E_T|^2 = \left| \sum_{n=1}^{5} A_n e^{i\phi_n} \right|^2 = \sum_{n=1}^{5} |A_n|^2 + 2 \sum_{j=1}^{5} \sum_{k=1\ k\neq j}^{5} A_j A_k \cos(\delta_{jk}) \tag{3}$$

where $\delta_{jk} = \varnothing_j - \varnothing_k$, represents the relative phase difference between two wave components, which is caused by the optical path length differences (OPLD) between different wave components, so $\delta_{jk} = \frac{2\pi OPLD_{jk}}{\lambda}$. Table A-1 in the Appendix Section A-2 shows the phase difference components where DC means direct current signal and AC means alternating current signal.

In Fig. 2, the curing front represents an imaginary interface between the liquid resin and the curing part. It encompasses the entire curing block containing intermediate phases between the liquid resin and the solid states. The cured height Z is the distance from the curing font to the top surface of the printed part, so the OPLD between E_3 and E_2 is calculated using Eq. 4, where $n(0) = n_s$, $n(Z) = n_{cf}$, n_m is the mean refractive index of the intermediate phases. With Eq. (4), all phase differences can be analyzed.

$$OPLD_{E_3-E_2} = \int_0^Z n(x)dx = n_m Z \tag{4}$$

In Appendix Table A-1, the oscillating phase difference values are caused by the changes of their corresponding OPLD which is related to the curing process. The camera-recorded signals, that is, the acquired ICM time series of data as described in Eq. 3 display components with varying frequency values along the DLP-VPP processing time. The instantaneous frequency (IF) is the rate of the phase change at the corresponding time instant. It is a pivotal parameter in time-frequency analysis, enabling extract the time-varying frequency from

nonstationary signals [30]. Assuming the process parameters of light intensity and material properties - n_l, n_s, n_{cf} are momentarily invariant, either cured height Z or effective or mean refractive index n_m change and are related to the IF. As illustrated in Table 1, the IF components are derived based on the information provided in Appendix Table A-1.

The high frequency f_1 and f_2 are removed during the data preprocessing when a low pass filter is applied (see Section 3.3.1), so only low frequency f can provide curing information. Therefore, the CMOS camera measured intensity I_M is modeled as the sum of the background intensity with low instantaneous frequency f in the multi-beam interference optics model, as shown in Eq. (5), where I_0 represents the average intensity, I_1 is the superposed intensity of interference beams with the same instantaneous frequency f, δ is the time varying phase shifting, $\varphi$is the superposed phase offset of interference beams with the same frequency, n_m is the mean refractive index of the cured part and n_l is the refractive index of the liquid resin, Z is the cured part thickness, λ is the green laser wavelength of 532 nm, ω is the instantaneous angular frequency and f is the instantaneous frequency [20].

$$I_M = I_0 + I_1\cos(\delta+\varphi) = I_0 + I_1\cos\left(\frac{4\pi(n_m-n_l)Z}{\lambda} + \frac{4\pi n_l H_C}{\lambda} + \varphi\right) \tag{5}$$

$$\omega = 2\pi f = \frac{d(\delta+\varphi)}{dt} = \frac{d\delta}{dt} = \frac{4\pi}{\lambda}\frac{d((n_m-n_l)\bullet Z)}{dt} + \frac{4\pi n_l}{\lambda}\frac{dH_C}{dt} \tag{6}$$

A differential form is derived from of Eq. (6). In this project, as only one layer is printed, the chamber height remains unchanged, indicated by $\frac{dH_C}{dt} = 0$, resulting in Eq. (7).

$$\frac{\mathrm{d}((n_m-n_l)\bullet Z)}{\mathrm{d}t} = \frac{\lambda\omega}{4\pi} = \frac{\lambda f}{2} \tag{7}$$

To evaluate the effective refractive index n_m of the cured part from the differential form in Eq. (7), the explicit ICM sensor model is generated using Euler's Method shown in Eq. (8) by assuming the cured height Z is constant:

$$n_m = n_l + \frac{\lambda}{2Z}\sum\nolimits_i T_i f_i \tag{8}$$

where T_i is the time step of integration, f_i is the instantaneous frequency in the i^{th} run of parameter estimation. The refractive index value of liquid resin n_l is 1.4723 based on [18]. It is noted that the cumulative sum term is essentially the total phase angle that has changed during the curing process.

3.2. ICM data preprocessing

The raw ICM data refers to the directly acquired video of interferograms that is recorded during ICM of a VPP process. For analyzing the ICM data, a set of secondary ICM data is obtained by extracting each individual pixel's time series of image grayscale values from the sequential interferogram frames in the acquired ICM video. The datasets of all pixels' time series of grayscale values are preprocessed to reduce the noise and screen high-quality ICM dataset, i.e., a subset of good ICM pixels that will vividly reflect curing dynamics and allow for accurate process measurement. This section presents the data cleaning process that is important to achieve an efficient and effective ICM measurement. Associated experiment results and discussions are presented in Section 4.2.

Table 1
Instantaneous frequency (IF) of the multi-beam interference optics model in ICM for DLP-VPP.

Instantaneous frequency (HZ)	Corresponding phase
$f_0 = 0$	δ_{21}, δ_{54}
$f_1 = \frac{2}{\lambda}\bullet\frac{\mathrm{d}(n_m \bullet Z)}{dt}$	δ_{31}, δ_{32}
$f_2 = \frac{2n_l}{\lambda}\bullet\frac{dH_C}{dt}, \frac{2n_l}{\lambda}\bullet\frac{\mathrm{d}Z}{dt}$	δ_{43}, δ_{53}
$f = \frac{2}{\lambda}\bullet\frac{\mathrm{d}((n_m-n_l)\bullet Z)}{dt} + \frac{2\pi n_l}{\lambda}\bullet\frac{dH_C}{dt}$	δ_{41}, δ_{51}, δ_{42}, δ_{52}

3.2.1. Noise filtering

During the polymerization process, the liquid resin is converted to solid part and thus resulting in shrinkage of the curing zone and movement of its surrounding liquid resin, which can induce noise in the ICM signal. To improve the signal-noise-ratio (SNR) of ICM time series of pixel grayscale data, multiple filters are used in the ICM data preprocessing. Firstly, a 5 × 5 image median filter is applied to each pixel's time series of grayscale values to reduce noise by replacing each pixel value with the median of its neighboring 25 pixels [23]. Then a low-pass filter with a cutoff frequency of 10 Hz, is used to remove high frequency noise peaks from the data. The chosen cutoff frequency (10 Hz in this case) is characterized from our experiment data and found to be sufficiently higher than typical maximal frequency values in DLP-ICM. A moving mean filter in MATLAB is used to further smooth the time curve of grayscales for allowing a better curve fitting later. The MATLAB function "movmean" calculates the mean of the values within a sliding window size.

3.2.2. Machine learning-based outlier detection

As those apparent and stochastic noise can be effectively filtered after using the methods in Section 3.3.1, there may be pixels who are subjected to certain systematic noise due to the DLP-VPP processing disturbances and the ICM camera sensing errors (see the challenges in Section 1.3). Especially given a large dataset of thousands of pixels' time series acquired during ICM across the entire print plane, there tends to exist a considerable portion of such bad pixels which are corrupted mainly by the systematic noise and cannot exhibit any quality signals to reflect the printing process characteristics. Those bad pixels are considered as outliers which don't carry any relevant DLP-VPP processing signatures. To clarify, the "bad pixel" or "outlier pixel" in this work refers to a DLP-VPP printed voxel that cannot be reliably used for ICM measurement purpose primarily due to the possible print process and sensor measurement noise including the DLP-VPP process disturbances by resin flow perturbance and build stage movement as well as the ICM sensor dysfunctions caused by electronics drift and overheat. Note that such bad or outlier pixel doesn't necessarily mean that the corresponding voxel is not adequately cured. Consequently, it is not worthwhile to conduct measurement analysis for these outlier pixels from the perspective of maintaining and enhancing data quality, computational efficiency, and measurement accuracy. Otherwise, such kind of measurements using bad pixels would require additional effort and resource to restore the genuine signal but still could significantly degrade the overall measurement performance. Overall, to ensure the accuracy of the estimated refractive index while saving computational effort, those bad pixels are marked as outliers and only those good pixels are used to solve the ICM sensor model for instantaneous frequency estimation and final calculations of refractive index and DoC.

To distinguish between good pixels and outliers, a robust and accurate machine learning-assisted algorithm is developed and implemented for pixel classification. The algorithm relies on identifying specific patterns in the time series of grayscale values, reflecting characteristic stages of VPP processing including incubation, exposure curing, dark curing, and resting. Please note that in this work "incubation" is used to refer to the commonly known "induction" period that describes the initial stage of photopolymerization reaction, only to be consistent with prior publications related to the ICM method [20,21]. Pixels that do not exhibit this pattern are considered as outliers. Pixel-wise time series of grayscale values are used for training and testing a machine learning model for ICM pixels triage. And this training and testing procedure involves using a dataset that is manually labeled. To ensure the integrity of the evaluation process, the entire dataset is split into three subsets: 60% for training, 10% for validation, and 30% for testing. This split is

performed to prevent data leakage and maintain the independence of the testing data, and the details of outlier detection are described in Section 4.2. A standard one-dimensional Residual Neural Network (ResNet) 18 is adopted [26], which is capable of effectively mitigating the vanishing gradient problem happened in deep neural network archetectures. By training the model using the labeled train set and testing its performance on the labeled unseen test data, the machine learning model can accurately classify pixels as either good pixel or outliers based on their time series grayscale values, allowing for robust and accurate detection of good pixels in the interferogram video and thus reliable ICM data analysis and measurement calculation. More details about the model development and results including the model training curve and testing confusion matrix in Section 4.2.

3.3. DLP-VPP process stages identification via ICM data mining

A typical DLP-VPP process comprises four stages as follows: (1) incubation (i.e., induction) or threshold when resin is absorbing and accumulating sufficient amount of light energy to commence curing; (2) exposure curing when the curing happens under the digital light irradiation; (3) dark curing when curing goes on due to residual catalysts (e.g., free radicals) and environmental conditions (e.g., ambient light) after the digital light exposure is turned off; and (4) resting stage when dark curing is completed. Ideally the ICM pixel-wise time series of grayscale should reflect these four distinct stages by displaying (1) flat line representing the initial background signal during the incubation; (2) oscillating waves reflecting the exposure curing dynamics; (3) relatively slower oscillating waves caused by the dark curing behavior; and (4) another flat line representing the final background signal while the entire curing process stops. In theory only the exposure curing and dark curing stages should be analyzed using the ICM model (Section 3.2) as the incubation stage and the resting stage don't involve any curing and should have zero contribution to the phase change. However, realistic ICM data contains various noise that present significant challenges for differentiating these intrinsic stages. For example, the flat segments during incubation and resting might exhibit noisy waves that would mislead one to consider it as curing waves in exposure curing or dark curing stage and overestimate the phase change.

As such, it is crucial to automatically and accurately distinguish these characteristic stages of a DLP-VPP process by segmenting its ICM time series before applying the ICM sensor model to estimate the metrics of curing (refractive index in this case). In practice, each segment of an ICM pixel time series has some distinct features that can be used to assist the curing stage identification. For the incubation stage, the liquid resin is exposed to light, but the exposure energy received hasn't reach the critical exposure energy for the chemical reaction to occur. In this stage, the ICM grayscale amplitude is relatively lower than the subsequent exposure curing stage, and the peak inside the incubation stage should not be counted for estimating refractive index. Hence, accurately determining the ending point of the incubation stage is crucial. During the exposure curing process, oscillations occur and there is a significant change in the grayscale values as captured by the AC component in our ICM model (Appendix Table A-1). The standard deviation and range of the data in a moving window within the curing stage should be much higher compared to the values in other stages. After the curing light is turned off, there is a period of dark curing characterized by the gradual widening of the oscillation peak until it reaches a certain width, indicating the resting stage. At the end of the dark curing phase, like the incubation stage, the standard deviation value and range are expected to decrease.

Inaccuracies in identifying curing stages can lead to erroneous phase angle estimation and thus inaccurate refractive index calculation. Therefore, it is important to set some empirical threshold values to identify the start and end of an effective curing period that includes exposure and dark curing stages. The time points of curing start and end are identified using some threshold values of ICM grayscale range and standard deviation. For enhancing the curing end point identification accuracy and robustness, a threshold value of cycle width is used. An "empty sample" experiment is conducted to characterize this threshold cycle width for detecting the curing end. Specifically, an ICM video is acquired while "printing" an empty sample by shinning UV light to a liquid resin that contains no initiators but only monomer. Thus, it records only the background signal due to the movement of liquid resin and other system noise. The average number of points for one cycle in this "empty sample" experiment is used as the reference value for marking the end of curing. When the number of points of the oscillation cycle exceeds the threshold number of points, the instantaneous frequency estimated by the ICM sensor model becomes nearly flat, indicating the end of curing reactions.

After the start and end time points of an effective curing period are determined, the instantaneous frequency values outside the effective curing period are assigned to be 0 to ensure that only relevant data within the effective curing period is considered for refractive index estimation later (elaborated in next subsection).

3.4. Solving the ICM sensor model with adaptive Fourier curve fitting of the effective curing period data

For each identified good pixel (Section 3.3), the segment of data series of the identified effective curing period (Section 3.4) is used to solve the sensor model as shown in Eq. 8, for evaluating the value of mean (i.e., effective) refractive index n_m at the corresponding pixel. The instantaneous frequency f_i for each time step is calculated using a one-term Fourier curve fitting algorithm with an exponentially weighted moving horizon window, as depicted in Eq. (9), where t is time, ω_i is the instantaneous angular frequency of i_{th} time step.

$$y = a_0 + a_1 \bullet \cos(\omega_i t) + b_1 \bullet \sin(\omega_i t) = a_0 + \sqrt{{a_1}^2 + {b_1}^2} \bullet \cos(\omega_i t + \theta)\omega_i = 2\pi f_i, \theta = \tan^{-1}(-\frac{b_1}{a_1}) \tag{9}$$

The instantaneous frequency is estimated for every 10 frames of an ICM video. As such, each time step in Eq. (9) involves 10 grayscale data points, which is 0.083 s given the sampling frequency of the camera of 120 Hz. After estimating the instantaneous frequency for each time step, numerical integration of the time sequence of instantaneous frequency is performed throughout the curing process to obtain the total phase angle change during the print.

As can be seen from the overall method above, it is important to ensure an accurate and robust estimation of each time step's instantaneous frequency. This is accomplished by using a moving window with weights exponentially decreasing from current to past time points. The initial window size, i.e., moving horizon length (MHL), is set to be 30 frames based on our initial runs of experiment data analysis. Exponentially decreasing weighting is applied to the data within each moving window with a parameter of "half-life", which is the width of data segment where the weight is decaying to one half. The half-life serves as a forgetting factor for the Fourier curve fitting to focus on the most recent data in order to accurately estimate the current instantaneous frequency. The choices of MHL and half-life depend on the VPP process speed and the ICM data acquisition rate and can use empirical values from prior experiment. Due to the distinct curing rates through a VPP process an adaptive WHL is developed to avoid improper MHL that could bring aliasing errors. Specifically, several candidate MHL values are used in the curve fitting and the fitting that results in the highest R-squared value is taken as the best fit. To save computational time, one can also apply the adaptive curve fitting only when the initial curve fitting results in a R-squared value less than certain threshold. In this work, when the R-squared value of the first run of curve fitting using a specified MHL is below 0.9, a while loop will be applied to change the window size to MHL* 0.5, MHL* 1, MHL* 1.5, MHL* 2 and MHL* 3

until find the curve fitting results with a $R^2 > 0.9$.

3.5. Correlation of the relationship between refractive index and degree of curing

The DoC measures the extent of the conversion of Carbon-Carbon double bonds (C═C) in the liquid monomer into Carbon-Carbon single bonds (C-C) in the cured polymer. As previously mentioned, since DoC exhibits a direct correlation with the refractive index of the as-printed parts, a correlation model between refractive index and DoC can be created to infer the DoC of DLP-VPP printed parts from the refractive index measured during the process by the ICM. To this end, the DoC values of printed samples should be characterized to train a good correlation model. In this work, a Fourier-transform infrared spectroscopy (FT-IR) (Vertex-70LS, Bruker, Billerica, MA) is used. The measurements are conducted using an attenuated total reflection (ATR) mode. In this mode, a total of 16 scans are performed with a resolution of 4 cm^{-1}, and the average of these scans is utilized to obtain the absorption spectrum. The DoC is determined by estimating the reduction in the absorbance peak area of the C═C bond peak at 1620$cm^{-1}$and 1635cm^{-1}. To normalize the peak absorbance value, the stable C═O stretching vibration peak at 1725 $cm^{-1}$is employed as an internal standard. The DoC is calculated using the Eq. (10).

$$DoC = 1 - \frac{\left[\frac{(A_{1620cm^{-1}} + A_{1635cm^{-1}})}{A_{1725cm^{-1}}}\right]_{polymer}}{\left[\frac{(A_{1620cm^{-1}} + A_{1635cm^{-1}})}{A_{1725cm^{-1}}}\right]_{resin}} \quad (10)$$

where $A_{1620cm^{-1}}$, $A_{1635cm^{-1}}$ and $A_{1725cm^{-1}}$ are the absorbance peak area at 1620cm^{-1}, 1635cm^{-1} and 1725cm^{-1}, respectively. $\left[\frac{(A_{1620cm^{-1}} + A_{1635cm^{-1}})}{A_{1725cm^{-1}}}\right]_{polymer}$ is the peak area ratio of sample and $\left[\frac{(A_{1620cm^{-1}} + A_{1635cm^{-1}})}{A_{1725cm^{-1}}}\right]_{resin}$ is the peak area ratio of unreacted resin.

The FT-IR-measured *DoC* and ICM-measured refractive index data are used to fit a regression model as shown in Eq. (11), which is the desired correlation model between the refractive index and *DoC* for the unfilled liquid resin [24].

$$DoC = a \bullet n_m + b \quad (11)$$

4. Results and discussion

4.1. Experiment design

Toward the goal of using the ICM method to measure DoC, a series of experiment is needed to gather sufficient data for creating a meaningful correlation model between DoC and refractive index. As such, a variety of samples are printed with different light intensities using our in-house DLP-VPP system and the corresponding print processes are monitored using our experimental ICM setup (see Section 2.2). The light mask for each sample is designed as a circle shape with a diameter of 2.5 mm. A single layer is printed with a layer thickness of 0.12 mm. The current ICM system can measure a sample thickness in the range of 0.01 mm to 0.18 mm. The maximum measurable sample thickness is limited by the power and coherent length of the green laser, which are described in Appendix Section A-1. Thicker samples tend to attenuate the ICM light resulting in weaker signals in ICM data. Thinner samples are easily broken during the post-build FTIR measurement. Therefore, the sample thickness is chosen to be 0.12 mm for this study. The light exposure time for each specimen is 5 s

Five sets of samples are printed on quartz glass slides using these different levels of light intensity as shown in Table 2. Three replications are conducted in each set for deriving a statistically significant refractive index-DoC correlation model as well as for evaluating the repeatability of the DLP process and the ICM measurement. Photos of representative printed samples are shown in Appendix Figure A-3. The power of the light mask is measured via an optical power meter (PM400, Thorlabs, NJ, USA) directly on the build platform with a projection window (Quart glass slide). The area of the projected light masks on the platform is measured by a digital caliper with a resolution of 0.01 mm. The light intensity is calculated by dividing the light power value over the light mask area. Note that the light intensity is modulated by changing the grayscale values of the 8-bit optical mask images from 0 to 255 of pixel, where 0 corresponds to a dark black pixel and 255 corresponds to a bright white pixel.

Table 2
DLP-VPP process setting.

Sample Set No.	Sample NO. (R: Replication)	UV Light intensity (mW/cm^2)	Mask Image Grayscale	Printing Substrate	Exposure time (s)
1	S1 R1, S1 R2, S1 R3	15	255	Quartz glass slide	5
2	S2 R1, S2 R2, S2 R3	11.63	195		
3	S3 R1, S3 R2, S3 R3	8.49	125		
4	S4 R1, S4 R2, S4 R3	5.77	63		
5	S5 R1, S5 R2, S5 R3	5.08	50		

4.2. ICM data acquisition and preprocessing

During the DLP-VPP processing of each sample as designed in Section 4.1, an ICM video of 1500 frames of interferogram is acquired with each frame having a resolution of 720 × 480 pixels (pixel size: 9.4 μm as calibrated in Table A-2 in Appendix Section A-3). Note the frame number of each ICM video might vary due to the manual operation of cameras. In this work, the region of interest (ROI) in each frame of interferogram contains about 90,000 pixels, resulting in 1.35×10^8 data points of timed grayscale value that need to be processed for a full-field pixel-wise time-resolved measurement analysis. This ICM data size can be even bigger while printing larger parts and using higher ICM frame rates. The ICM data can also be noisy, necessitating preprocessing for cleaning the data and enhancing the calculation efficiency and accuracy.

As described in Section 3.3, a machine learning model is used to detect outliers and only good pixels are used to do the parameter estimation to provide information about refractive index. To provide a sufficient dataset for training and testing the machine learning model, good pixels and bad pixels are manually labelled based on both theory and experimental observations that good pixels should exhibit distinct features in their time series of intensity values that can reflect vividly the characteristic stages of a DLP-VPP process as introduced in Section 3.4. Fig. 3 shows some representative good pixels and bad pixels from S5 R3 (Replication 3). Good pixels are expected to exhibit a high SNR as shown in Fig. 3 (bottom), starting with a relatively flat line during the induction time, followed by oscillating cycles that gradually become wider until they eventually flatten out corresponding to the curing period. However, bad pixels as shown in Fig. 3 (top) exhibit a lower value of SNR, causing difficulty to identify the start point and end point of the curing period. The amplitude in the bad pixels is relatively small compared to the filtered grayscale values of the good pixels and cannot provide useful information about the process dynamics.

A total of 946 pixels selected from Sample Sets 1–5 are manually labelled and used as the dataset to train and test a machine learning model. As mentioned in 3.3.2, 60% of the dataset is used for training, 10% for validation, and 30% for testing. Thus, 567 pixels are used for training, 95 pixels are used for validation, and the remaining 284 pixels are used as the unseen test data set. Cross entropy loss function is used with the adaptive moment estimation algorithm (ADAM) for optimization. Table 3 shows the confusion matrix of the developed machine

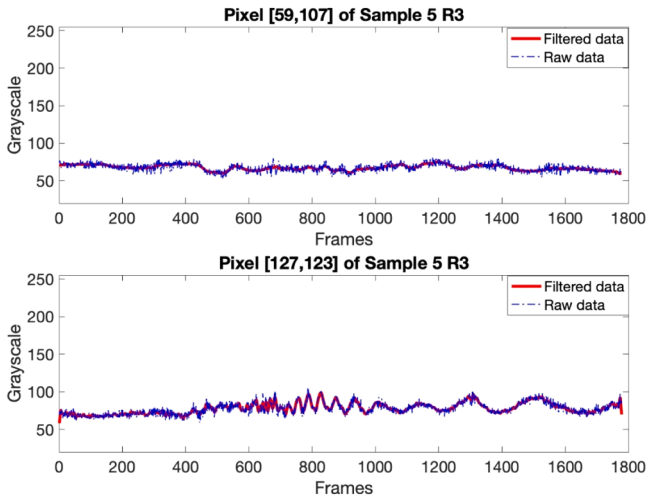

Fig. 3. Representative raw data and filtered time series of grayscale value for a bad pixel (top) and a good pixel (bottom) in Sample Set 5 Replication 3.

learning model, which presentss the performance of the classification model on the unseen dataset. Within the confusion matrix, True Positive (TP) represents the accurate classification of good pixels as good by the ML model, False Positive (FP) signifies the erroneous identification of bad pixels as good pixels by the ML model, False Negative (FN) indicates the misclassification of good pixels as outliers by the ML model, and True Negative (TN) stands for the precise identification of outliers as such by the ML model. The evaluation is conducted on the unseen dataset including 284 pixels, consisting of 177 good pixels and 107 bad pixels (outliers). Out of the 177 good pixels, the model correctly classified 173 as good and misclassified 4 as bad. For the 107 outliers, the model classified all of them correctly with bad pixel label.

Using these results, we can further evaluate other model performance metrics such as accuracy, precision, recall and F1 score.

$$\text{Accuracy} = \frac{\text{TN} + \text{TP}}{\text{TN} + \text{TP} + \text{FN} + \text{FP}} = 98.59\%$$

$$\text{Precision} = \frac{\text{TP}}{\text{TP} + \text{FP}} = 100.00\%$$

$$\text{Recall} = \frac{\text{TP}}{\text{TP} + \text{FN}} = 97.74\%$$

$$\text{F1} - \text{score} = 2 * \frac{\text{Precision} * \text{recall}}{\text{precision} + \text{recall}} = 98.86\%$$

Before the outlier detection, the ROI for each sample is selected according to the location of cured sample shown on the recorded ICM video. Then the developed machine learning mode is used to classify all the pixels throughout the entire ROI. The identified good pixels are used for estimating the effective refractive index within that ROI. The outlier detection results are shown in Fig. 4. For each sample, it becomes evident that the peripheral region of the cured area exhibits more good pixels compared to the central region. This observed phenomenon can be attributed to the fact that voxels within the central region are covered by a relatively higher volume of liquid resin in contrast to those situated at the periphery. This is because we print the samples using droplets of resins on the build platform. As a result, the increased presence of liquid resin leads to greater attenuation of the green laser, consequently yielding a weaker interference signal. This issue of non-uniform ICM signal may be mitigated in practical DLP-VPP processes where a vat of resin is used. Besides, most of the samples display a clear circular pattern of good pixels indicating that the ICM system can capture the shape (circle as used in this work) of curing area well. It shows that ICM can be used to measure the geometry including lateral dimensions and cross-sectional shape of an in-process part. Although this work is focused on measuring refractive index and DoC, additional investigation on the geometry measurement capability of ICM is still conducted to show its versatility. For more details, please refer to Appendix Section A-3, where the scaling factor between the ICM image pixel size and the printed part pixel size is characterized. Both dimensions and angles are measured using the in-situ ICM and compared to ex-situ measurement results, showing a good agreement.

4.3. DLP-VPP process stages identification

To identify curing stages, the standard deviation and range are estimated for every 10 frames of ICM camera data and compared with empirical critical values. Distinct critical values are utilized, as samples from Experiment Sets 1, 2 and 3 exhibit higher amplitude than samples from Sets 4 and 5. For samples in Sets 1, 2, and 3, the critical standard deviation is set to be 5 and the critical range is 10. For samples in Sets 4 and 5, the critical standard deviation is set to be 3 and the critical range is 5. To enhance the robustness of identifying the endpoint of the curing periods, a critical cycle width is used. This critical value is determined through the "empty sample" experiment as described in Section 3.3, where the reference background signal is characterized to be 200 points per cycle corresponding to a time duration of 1.667 s. With all the characterized critical values, the curing start and end time points are labeled for each good pixel's time sequence of grayscale values.

The Fig. 5 shows representative pixels from each sample set as designed in Section 4.1. The developed stage identification method is utilized to determine the start point and end point of the curing stage. The curing start point also indicates the end of the induction stage, signifying the moment when the transition from liquid resin to solid

Table 3
Confusion matrix of the machine learning model for identifying good pixels and outliers.

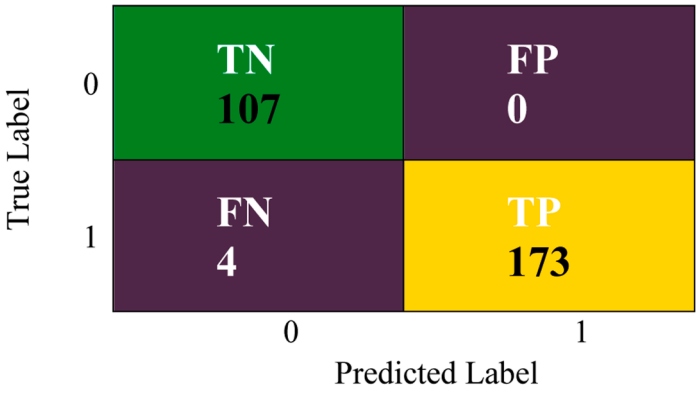

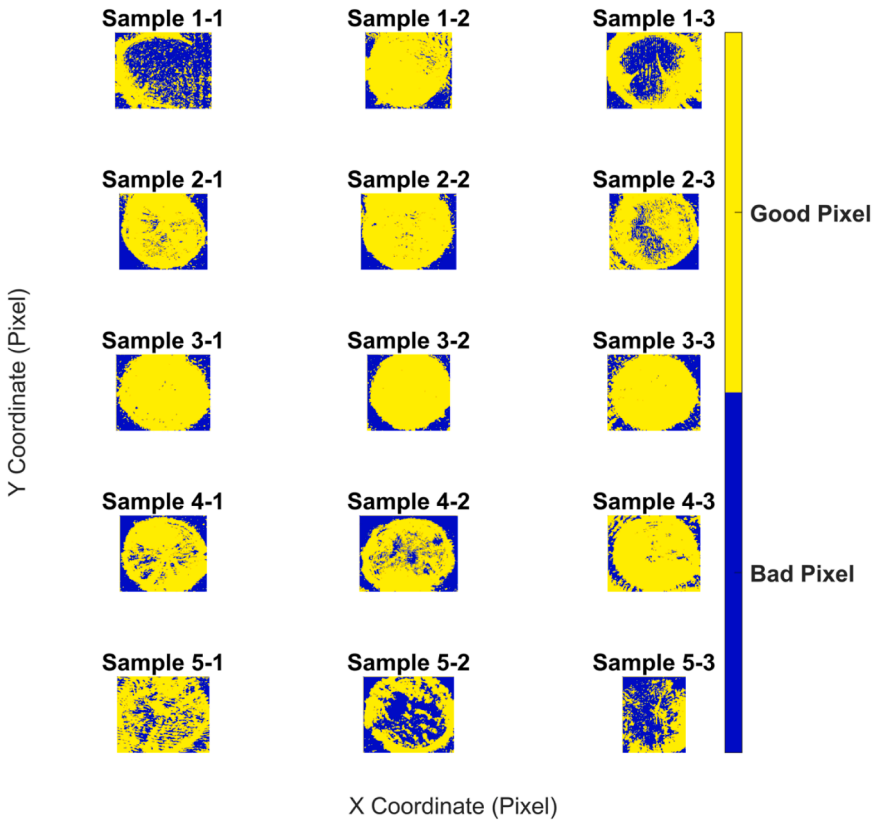

Fig. 4. Results of the machine learning-based outlier detection at a region of interest for each sample ("Sample 1–2″ means the sample from Sample Set 1 Replication 2, etc.). Yellow color shows good pixels and blue color shows bad pixels. From top to bottom, the light intensity gradually decreases. For each light intensity, three replicates are printed (for details, see the experiment design in Section 4.1).

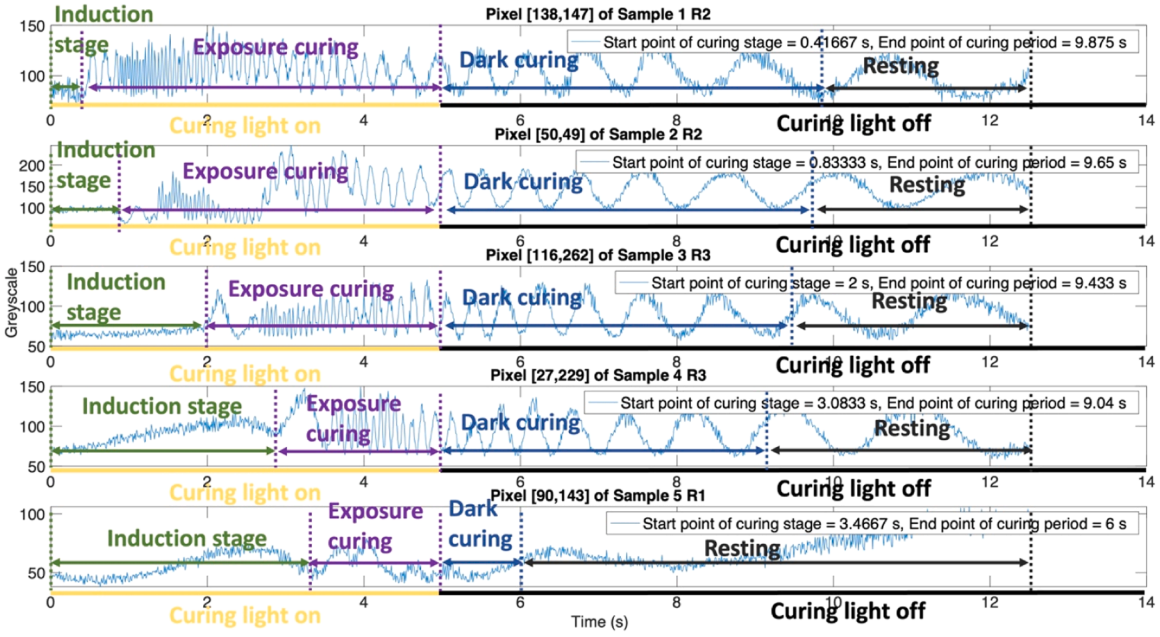

Fig. 5. Representative results of identifying the effective curing, i.e., the start of exposure curing and the end of dark curing for Samples 1–5 cured in the designed Experiment Sets 1–5, respectively. From top to bottom, the decreasing amplitude of ICM signal (i.e., pixel grayscale value) well reflects the fact that the DLP-VPP processing light intensity is decreasing in the different sets of experiment.

polymer becomes observable by the ICM. The curing end point is the termination of dark curing, after which the curing signal is like a background signal and cannot provide useful information about curing. From top to bottom plots, light intensity is decreasing and the corresponding incubation time is increased.

Table 4 shows a statistic of the average value of curing start point and end point for each experiment set. As expected, an increase in DLP-VPP processing light intensity correlates to a reduction in the required

induction time. Furthermore, the result reveals that a higher light intensity is associated with a prolonged dark curing stage. This phenomenon can be attributed to the fact that elevated light intensity results in accumulation of more light exposure energy within the same exposure duration, thereby extending the duration of the dark curing stage. Our ICM observations conform to the intuitive understanding about the DLP-VPP mechanisms, enhancing the confidence of using ICM to accurately measure the curing process dynamics. Herein, we demonstrate a successful identification of effective curing stages using the method developed in Section 3.4. This greatly helps guarantee an accurate solution of the ICM model evaluation in next subsection.

4.4. Estimating the effective refractive index of DLP-VP printed parts via ICM sensor data analytics

The adaptive curve fitting method as introduced in Section 3.5 is used to calculate the time-varying instantaneous frequency out of the identified curing period's time series of grayscale value for each detected good pixel.

Fig. 6(a) shows the representative results of a sample pixel's time curve of estimated instantaneous frequency and corresponding curve fitting results of time series grayscale from each sample set that uses different levels of exposure light intensity. Fig. 6(b) displays the evolving refractive index during the printing process. It clearly shows that a higher exposure intensity used in the DLP-VPP process would lead to a shorter induction time, a higher instantaneous frequency that indicates faster curing during the curing period, and a longer dark curing. This result also proves that ICM data and results can reveal the actual process dynamics of DLP-VPP, which are not attainable by current means.

The refractive index values are calculated by plugging the estimated instantaneous frequency values into the ICM sensor model (Section 3.2). The results for Sample Sets 1–5 are summarized in Appendix Table A-3. Several statistical measures have been estimated including the mean, median, standard deviation, range (maximum - minimum), and the robust mean and robust sigma. The robust method is using "robustcov" command in MATLAB to estimate the mean and covariance values while reducing the effects of outliers on the average. According to Appendix Table A-3, the average value estimated by the robust method is lower than the mean values calculated by the traditional method for each sample, and the median value is closer to the robust mean value than the traditional mean results. It can be observed that Sample Set 1 have higher refractive index values than other samples sets, showing that increasing light intensity results in higher values of refractive index. On the other hand, Sample Sets 1,2, and 3 have larger range values than Sample Set 4 and 5. The reason for this phenomenon can be attributed to more diffusion of generated radicals to unexposed area during the curing process and the consequential more over-curing in those unexposed regions. This curing process variation is manifested by the distinct refractive index values, validating that the developed ICM method is capable of capturing the spatial distribution of process dynamics. However, ex-situ quantitative characterization of the refractive index of cured sample can be performed using standard reflectometry to directly validate the ICM-estimated refractive index in the future.

Table 4
Curing stage identification results: average duration of induction and dark curing for each sample set (exposure time: 5 s).

Sample Set No.	DLP-VPP Processing Light Intensity (mW/cm^2)	Average induction time (s)	Average dark curing time (s)
1	15.00	0.49	4.23
2	11.63	0.81	4.21
3	8.49	2.03	3.26
4	5.77	2.99	2.80
5	5.08	3.53	1.53

Fig. 7 shows the boxplot of all good pixels identified in all the five samples sets that are measured using the ICM method, allowing for a comprehensive comparison of the refractive index measurement results. Meanwhile, the left-side vertical axis shows the robust mean value of each sample set, and the right-side vertical axis shows the average DoC of each sample set. The blue star marker denotes the mean value of the average refractive index of each replication for Sample set 1–5. The trend is that higher ICM measured refractive index correlates to a higher DoC. This relationship is further investigated in the next subsection.

4.5. Inferring the degree of curing of DLP-VPP printed parts using refractive index measured by ICM

Table A-4 in Appendix Section A-5 presents the ICM-measured refractive index and FTIR-measured DoC for each sample. It indicates a positive correlation between DoC and refractive index, where a higher degree of cure results in a higher refractive index. A refractive index-DoC correlation model is developed by curve fitting of Eq. (11) using the DoC and refractive index values of the first two replications in each sample set, as shown in Fig. 8. The fitted correlation model is DoC $= 16.934 \bullet n_m - 24.963$, and the R^2 of the curve fitting is 0.8523. The estimated correlation model is tested on all the unseen data – the third replication in each sample set. Table A-5 in Appendix Section A-5 shows the performance of the developed correlation model on predicting DoC of printed parts in Replication 3 for each sample set. The prediction error is calculated as the absolute value of (predicted DoC – FTIR measured DoC) / FTIR measured DoC. The average error for all 5 samples is 16.2%. In this work, the correlation model is established using a linear model, as per Howard's work [24]. In Fig. 8, it's observed that once the DoC reaches 50%, the change in refractive index with the increasing DoC becomes relatively minor. On one hand, it is worth noting that the limited sample number could significantly affect the model development and accuracy. On the other hand, the observation from Fig. 8 seems to be consistent with Aloui's work, which investigates the evolution of refractive index in a set of commercial acrylic resins during photopolymerization [31]. Their results indicate that refractive index would linearly increase with DoC when the material is not in the glassy state and remain constant above a certain DoC threshold even as the reaction continues. This phenomenon might be attributed to the heavy dependence of refractive index on material density, which however tends to be constant after the material reaches a certain DoC value [14,31,32]. To conclude, while a simple linear model proves to be reasonably effective for a specified range of DoC, its applicability is constrained by specific limits determined by the nuanced relationship with the material's density, refractive index, and other properties such as molecular-level structures. In the future, more experiment data and machine learning models can be used to comprehend and capture the intricate relationships between the refractive index and DoC, thereby enhancing the model prediction accuracy.

With the developed correlation model, the DoC of each voxel can be predicted via the ICM estimated refractive index with a decent accuracy. The time-varying DoC values of representative pixels from each sample set are shown in Fig. 9. It vividly reveals that increasing curing light intensity (from S5 to S1) leads to less incubation time and higher DoC at the same exposure time. The prediction accuracy can be further improved by developing an enhanced correlation model as discussed above Fig. 8.

5. Conclusion

In this work, we develop a cost-effective, non-destructive, full-field, multi-modality, and real-time in-situ interferometric curing monitoring (ICM) system for spatiotemporally characterizing the process dynamics and material properties during the DLP-based VPP (DLP-VPP) processes with a focus on measuring the refractive index and estimating the degree of curing. While the results may appear preliminary due to the

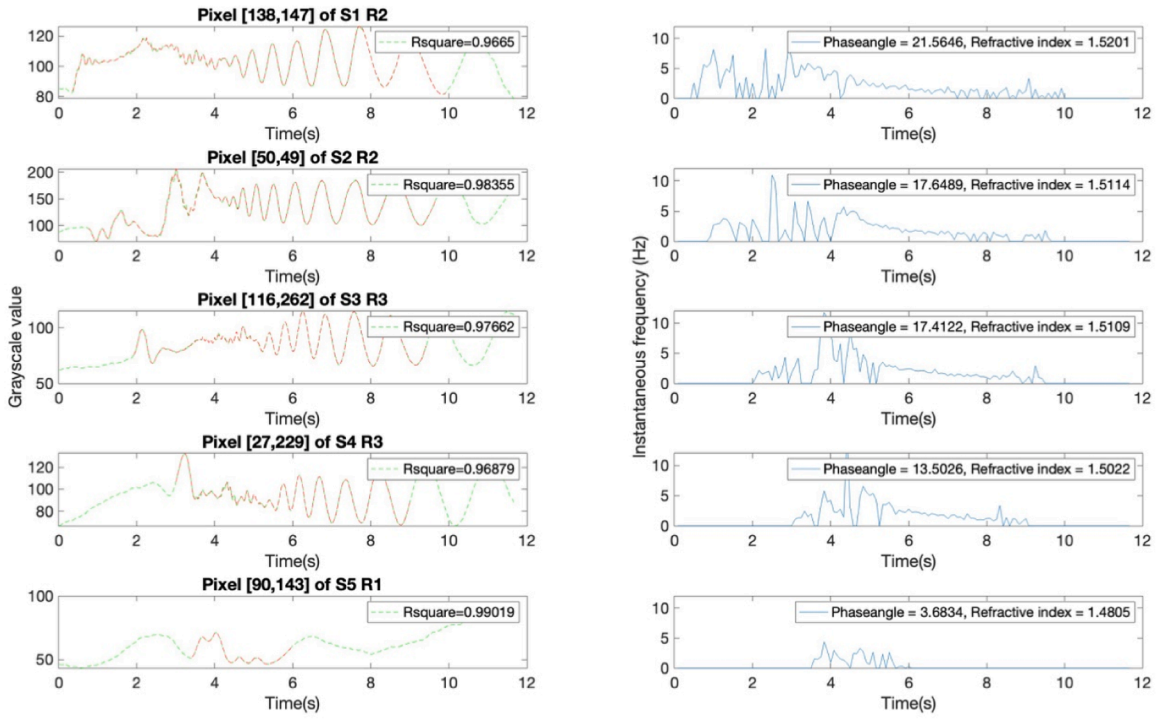

(a)

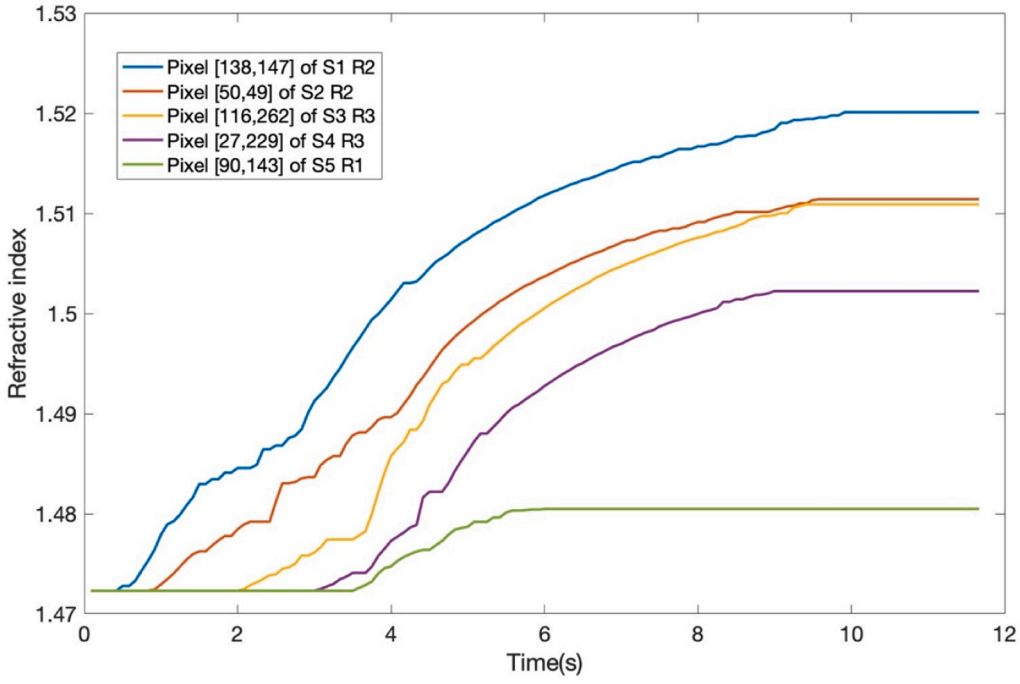

(b)

Fig. 6. (a) Representative curve fitting results of time series of grayscale value (left) and corresponding instantaneous frequency (right) estimated for a typical sample in Experiment Sets 1–5, respectively. (b) Representative time curves of evolving refractive index for these samples.

constraints of a limited experiment, it is crucial to emphasize the significant development, articulation, and establishment of the overall methodological framework for DLP-specific ICM. This framework has been meticulously laid out, and a proof of concept has been successfully demonstrated towards achieving the intended goals of understanding, controlling, and enhancing general DLP-VPP processes.

The significant outcomes are summarized as follows.

- First, an explicit, physics ICM sensor model is derived based on multi-beam optical interference in the context of general DLP-VPP that involves a moving building stage and print head, which affects ICM optical sensing path.

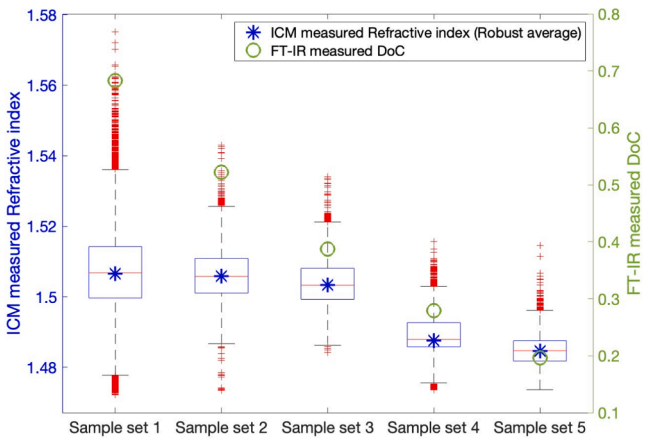

Fig. 7. Boxplot of refractive index of Sample Set 1 to Sample Set 5. For each sample set, the refractive index values of all good pixels identified in all three replications are calculated and utilized to calculate the statistics values in the plot.

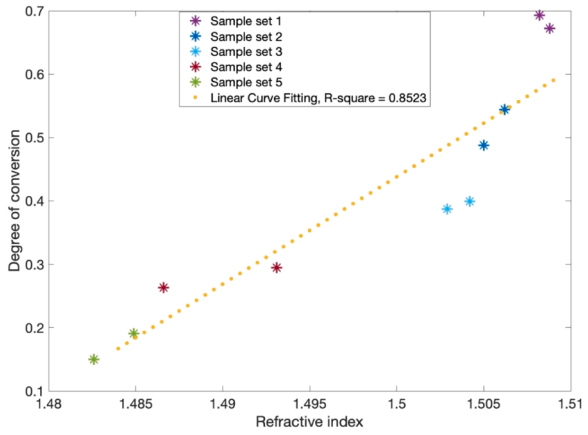

Fig. 8. Correlation model of refractive index and DoC.

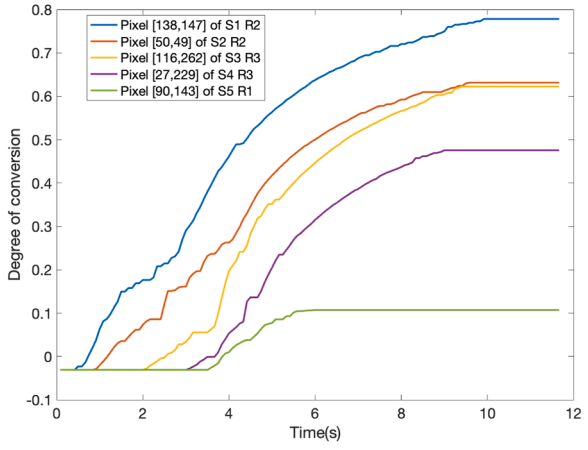

Fig. 9. Predicted DoC evolution during the DLP printing of the representative samples in Experiment Sets 1–5, respectively.

- Second, machine learning-aided sensor data processing and analytics methods are developed to address the unique challenge in DLP-VPP-specific ICM. Especially, this ICM approach is sensitive to the interferogram image noise which are worsened by the possible optics misalignment, limited light transmission, resin flow, and process disturbance in the scenario of DLP-VPP. A machine learning-based outlier detection method is developed using our manually labeled pixels based on our substantial analysis of ICM image pixels' time sequences of intensity values. The trained model can successfully identify good pixels that have high signal-to-noise ratio and thus can be used for accurately estimating refractive index and DoC.
- The developed ICM system and methods are demonstrated to be able to reflect the curing process dynamics (i.e., time-curve of instantaneous frequency that indicates the curing speed through the print process) and capture the material properties changes (i.e., time-curves of refractive index and DoC of as-printed parts) in response to the different DLP-VPP process settings (i.e., changes in the exposure intensity). Meanwhile, ICM can also measure the geometry (e.g., lateral dimensions and shapes) of printed parts during the process, making it a versatile method for full-field and multi-modality monitoring of a DLP-VPP process and its product properties.
- It is worth noting that the methods developed above are readily applicable to measuring the DLP-VPP process and part properties in real time with online data analytics capability as demonstrated in the previous work of Zhao et al. [22]. Therefore, the developed correlation model can estimate the DoC of an as-printed part not only after a DLP-VPP process as demonstrated in this work but also during the process in real time by analyzing online the associated ICM data via implementing the developed methodological framework.

In the future, ex-situ characterization of printed parts' refractive index will be conducted to directly validate the ICM-measured refractive index. More experiment data will be collected to enhance the transferability and prediction accuracy of the refractive index-DoC correlation model. Moreover, a real-time ICM of various DLP-VPP processes and print properties will be demonstrated. A close-loop feedback control of the photopolymerization process will be developed, thereby improving the accuracy and reproducibility of DLP-VPP processes.

CRediT authorship contribution statement

Yue Zhang: Methodology, Investigation (Experiments and Data acquisition), Data Analysis, Writing-Original draft preparation & Editing, Visualization and Supervision. **Haolin Zhang:** Methodology, Investigation (Experiments and Data acquisition), Data Analysis, Writing-Original draft preparation & Editing, Visualization. **Xiayun Zhao:** Conceptualization, Methodology, Resources, Writing – Draft, Review & Editing, Supervision, Funding acquisition, and Project administration.

Declaration of Competing Interest

The authors declare that they have no known competing financial interests or personal relationships that could have appeared to influence the work reported in this paper.

Data Availability

Data will be made available on request.

Acknowledgements

We acknowledge the fundings from 1) the National Science Foundation Future Manufacturing program (Award: CMMI-2134447) and 2) the National Science Foundation Faculty Early Career Development program (CAREER Award: CMMI-2238557). Any opinions, findings, and conclusions or recommendations expressed in this publication are those of the authors and do not necessarily reflect the views of the National Science Foundation. This work also used the National Science Foundation-funded Advanced Cyberinfrastructure Coordination Ecosystem: Services & Support (ACCESS) resource - Pittsburgh

Supercomputing Center Bridges GPU and Storage through allocation MCH210015. The ACCESS resources are used for accelerating the machine learning process of large amount of ICM data to identify good pixels with high signal-to-noise ratio. The authors would like to thank Dr. Chaitanya Vallabh and Heyang Zhang for their help on ZIP-AM lab's VPP setup.

Appendix

Section A-1: Coherent length calculation

To determine the range of the thickness of the cured sample, the coherence length is calculated based on the wavelength spectrum of green laser, as shown in Figure A-1.

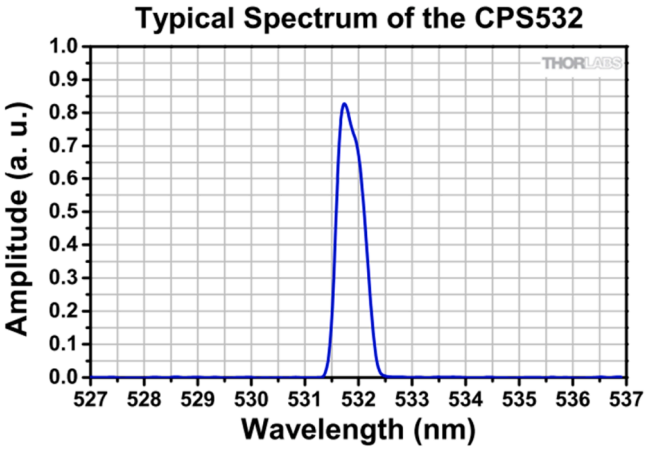

Fig. A-1. Wavelength of green laser (obtained from Throlbas.).

.

More challenges arise from the fact that the coherent length of a CIM light source could become short as the part grows thicker especially in the case of printing macroscopic parts. The coherent length (L_c) of the ICM light beam is estimated using Eq. (A-1), where λ is the center of the range of wavelength of the green laser and $\Delta\lambda$ is the total range of the wavelength. The limited $L_c$will lead to complex signals that cofound signatures from the entire part whose optical length tends to be larger than L_c and the fresh layers that are within L_c. This will require more complex signal analysis such as time-windowed frequency-domain method.

$$L_c = \lambda^2 \Big/ \Delta\lambda \approx \frac{(532nm)^2}{2 \bullet (0.75nm)} \sim = 188um \tag{A-1}$$

Section A-2: ICM sensor modeling

Table A-1
Phase difference component analysis of the multi-beam interference optics model in DLP-VPP ICM.

No.	Phase difference	Source beams	Role in the ICM time series data
1	$\delta_{21} = \frac{4\pi}{\lambda} n_h H_h$	E_1, E_2	Constant DC term
2	$\delta_{31} = \frac{4\pi}{\lambda} n_m Z + \delta_{21}$	E_1, E_3	Oscillating AC term
3	$\delta_{41} = \frac{4\pi}{\lambda}(n_m - n_l)Z + \frac{4\pi}{\lambda} n_l H_C + \delta_{21}$	E_1, E_4	Oscillating AC term
4	$\delta_{51} = \frac{4\pi}{\lambda}(n_m - n_l)Z + \frac{4\pi}{\lambda} n_l H_C + \delta_{21} + \frac{4\pi}{\lambda} n_p H_p$	E_1, E_5	Oscillating AC term
5	$\delta_{32} = \frac{4\pi}{\lambda} n_m Z$	E_2, E_3	Oscillating AC term
6	$\delta_{42} = \frac{4\pi}{\lambda}(n_m - n_l)Z + \frac{4\pi}{\lambda} n_l H_C$	E_2, E_4	Oscillating AC term
7	$\delta_{52} = \frac{4\pi}{\lambda}(n_m - n_l)Z + \frac{4\pi}{\lambda} n_l H_C + \frac{4\pi}{\lambda} n_p H_p$	E_2, E_5	Oscillating AC term
8	$\delta_{43} = -\frac{4\pi}{\lambda} n_l Z + \frac{4\pi}{\lambda} n_l H_C$	E_3, E_4	Oscillating AC term
9	$\delta_{53} = -\frac{4\pi}{\lambda} n_l Z + \frac{4\pi}{\lambda} n_l H_C + \frac{4\pi}{\lambda} n_p H_p$	E_3, E_5	Oscillating AC term
10	$\delta_{54} = \frac{4\pi}{\lambda} n_p H_p$	E_4, E_5	Constant DC term

Section A-3: Calibration of scaling factor between pixel and physical printed part (lateral dimensional size of pixel)

To obtain the actual lateral voxel size, calibration is conducted. Three samples with different shapes and sizes are used to minimize the error. All the patterns are cut by black tape and the dimensions are measured by caliper. The pattern is placed at the same projection window and the print head is placed at same initial position as resin printing, then the recorded interference pattern is analyzed. The pixel number and angle are calculated based on the horizontal and vertical pixel numbers. Figure A-2 shows the designed calibration pattern as well as the captured interference pattern. The calibration results are summarized in the table below. According to the calibration results, the deformation in the angle shift between the actual sample and the ICM-captured interference pattern is small.

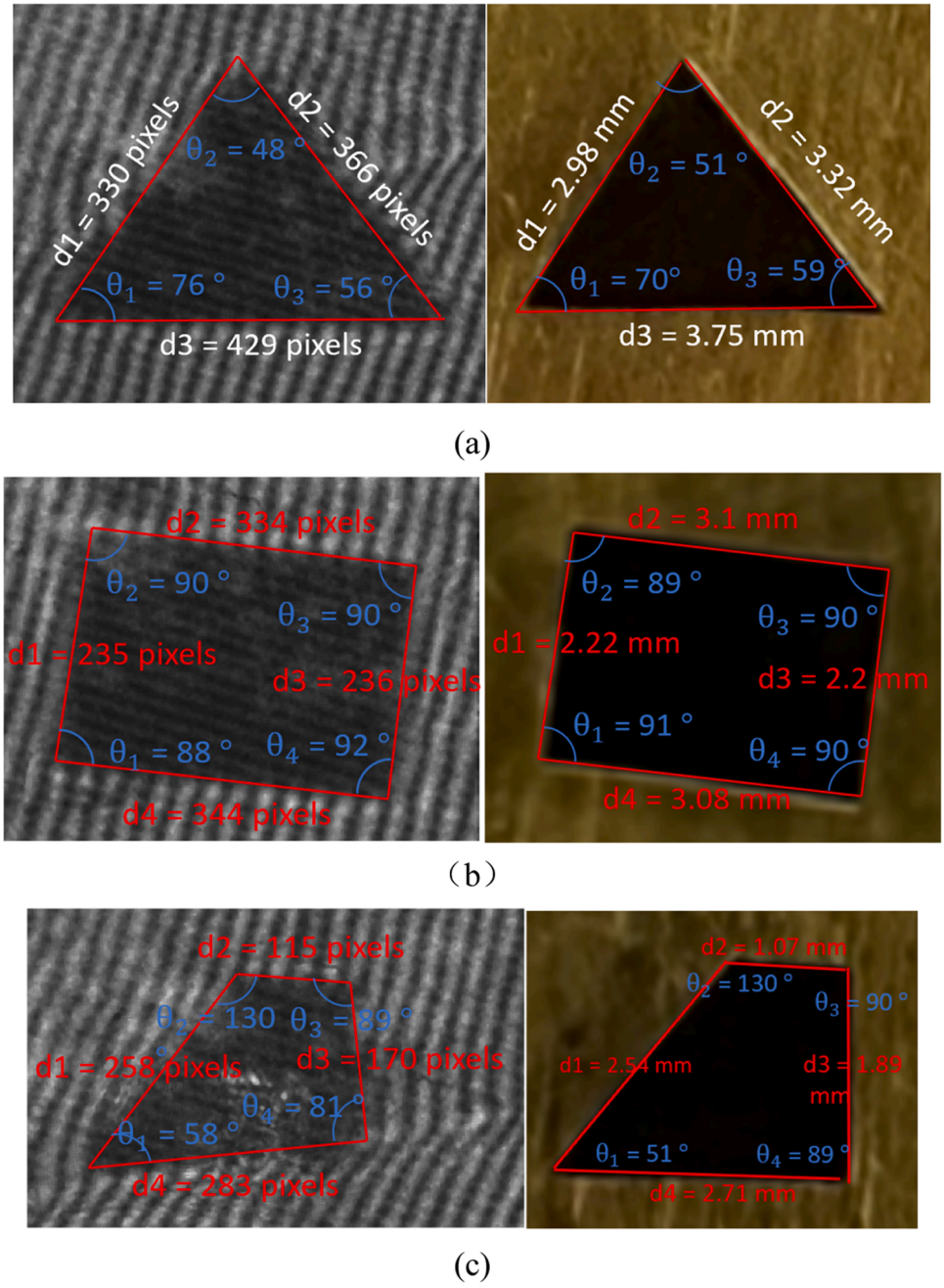

Fig. A-2. Left: ICM recorded interferogram of (a) triangle, (b) rectangle, (c) trapezoidal. Right: photo of actual object of (a) triangle, (b) rectangle, (c) trapezoidal.

.

The table below shows the results of calculated pixel size and angle distortion. The relative ICM angle error in the unit of percentage is calculated by the ratio of absolute value of (actual angle – ICM measured angle) over actual angle.

Table A-2
Calibration results (Note: ICM angle error unit is percentage).

		Label	Caliper measured size (mm)	ICM measured pixel number	um/ pixel	Actual angle (degrees)	ICM measured angle (degrees)	ICM angle error
Triangle	left	d1	2.98	330	9.04	70	76	8.85
	right	d2	3.32	366	9.07	51	48	5.96
	bottom	d3	3.75	429	8.74	59	56	5.28
Rectangle	left	d1	2.22	235	9.45	91	87.5	3.69
	top	d2	3.1	334	9.28	89	90	1.01
	right	d3	2.2	236	9.34	90	90	0.32
	bottom	d4	3.08	344	8.94	90	92	2.5
Trapezoid	left	d1	2.54	258	9.85	51	58	12.78
	top	d2	1.07	115	9.28	89	81	8.27
	right	d3	1.89	170	11.09	90	89	1.08
	bottom	d4	2.71	283	9.57	130	132	2.07
Average					9.42			4.71
Standard Deviation					0.6			3.76

Section A-4: Sample photos and estimated refractive index results

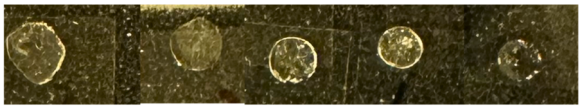

Fig. A-3. Representative samples from the five experiment sets as shown in Table 1, respectively. (From left to right: Sample 1, Sample 2, Sample 3, Sample 4, Sample 5).

Table A-3
Effective refractive index of DLP-VPP printed parts estimated using the developed ICM method.

Sample Set		Robust mean	Robust sigma	Mean	Standard deviation	Median	Range
1	R1	1.5082	4.1827E-04	1.5091	0.0202	1.5075	0.1028
	R2	1.5088	5.3327E-05	1.5092	0.0074	1.5089	0.0538
	R3	1.5033	6.4755E-05	1.5036	0.0081	1.5032	0.0654
2	R1	1.5050	5.7014E-05	1.5054	0.0081	1.5050	0.0695
	R2	1.5062	4.3046E-05	1.5066	0.0066	1.5063	0.0447
	R3	1.5063	6.1305E-05	1.5071	0.0079	1.5065	0.0523
3	R1	1.5042	4.0533E-05	1.5046	0.0064	1.5042	0.0491
	R2	1.5029	4.1947E-05	1.5037	0.0066	1.5030	0.0499
	R3	1.5029	4.0197E-05	1.5036	0.0064	1.5028	0.0477
4	R1	1.4866	1.2467E-05	1.4867	0.0042	1.4865	0.0309
	R2	1.4931	3.2842E-05	1.4931	0.0059	1.4931	0.0421
	R3	1.4869	5.0112E-06	1.4866	0.0035	1.4868	0.0301
5	R1	1.4826	1.2194E-05	1.4833	0.0038	1.4827	0.0272
	R2	1.4849	2.0932E-05	1.4856	0.0047	1.4850	0.0314
	R3	1.4866	9.2690E-06	1.4869	0.0042	1.4866	0.0406

Section A-5: Estimating the degree of curing using the ICM-measured refractive index

Table A-4
Comparison of ICM-estimated refractive index and FTIR-measured DoC.

Sample Set NO.	Sample NO.	ICM-measured refractive index (Robust mean)	FTIR-measured DoC
1	S1 R1	1.5082	0.693
	S1 R2	1.5088	0.672
	S1 R3	1.5033	0.555
2	S2 R1	1.505	0.488
	S2 R2	1.5062	0.544
	S2 R3	1.5063	0.534
3	S3 R1	1.5042	0.399
	S3 R2	1.5029	0.387
	S3 R3	1.5029	0.375
4	S4 R1	1.4866	0.263
	S4 R2	1.4931	0.295
	S4 R3	1.4869	0.28
5	S5 R1	1.4826	0.15
	S5 R2	1.4849	0.191
	S5 R3	1.4866	0.248

Table A-5
Prediction results of the correlation model.

Sample NO.	ICM measured refractive index	FTIR measured DoC	ICM Predicted DoC	Prediction Error %
S1 R3	1.5033	0.555	0.494	10.991
S2 R3	1.5063	0.534	0.545	-2.060
S3 R3	1.5029	0.375	0.487	-29.867
S4 R3	1.4869	0.280	0.216	22.857
S5 R3	1.4866	0.248	0.211	14.919

References

[1] A. Bagheri, J. Jin, Photopolymerization in 3D Printing, ACS Appl. Polym. Mater. 1 (4) (2019) 593–611.
[2] M. Pagac, J. Hajnys, Q.-P. Ma, L. Jancar, J. Jansa, P. Štefek, J. Mesicek, A review of vat photopolymerization technology: materials, applications, challenges, and future trends of 3D printing, Polymers 13 (2021) 598.
[3] B.E. Kelly, I. Bhattacharya, H. Heidari, M. Shusteff, C.M. Spadaccini, H.K. Taylor, Lawrence Livermore National Lab, Volumetric additive manufacturing via tomographic reconstruction, Science 363 (2019) 1075–1079.
[4] J.R. Tumbleston, D. Shirvanyants, N. Ermoshkin, R. Januszewicz, A.R. Johnson, D. Kelly, K. Chen, R. Pinschmidt, J.P. Rolland, A. Ermoshkin, E.T. Samulski, J. M. DeSimone, Continuous liquid interface production of 3D objects, Science 347 (6228) (2015) 1349–1352.
[5] C. Chung Li, J. Toombs, H. Taylor, Tomographic color Schlieren refractive index mapping for computed axial lithography, Symp. . Comput. Fabr. (2020) 1–7.
[6] A. Chivate, C. Zhou, Enhanced schlieren system for in situ observation of dynamic light–resin interactions in projection-based stereolithography process, J. Manuf. Sci. Eng. 145 (8) (2023).
[7] M.L. Dong, K.G. Goyal, B.W. Worth, S.S. Makkar, W.R. Calhoun, L.M. Bali, S. Bali, Accurate in situ measurement of complex refractive index and particle size in intralipid emulsions, J. Biomed. Opt. 18 (8) (2013) 87003.
[8] C.I. Higgins, Digital light processing in a hybrid atomic force microscope: in situ, nanoscale characterzation of the printing process, Addit. Manuf. 38 (2020).
[9] T. Scherzer, U. Decker, Real-time FTIR–ATR spectroscopy to study the kinetics of ultrafast photopolymerization reactions induced by monochromatic UV light, Vib. Spectrosc. 19 (2) (1999) 385–398.
[10] T. Hafkamp, G. van Baars, B. de Jager, P. Etman, A feasibility study on process monitoring and control in vat photopolymerization of ceramics, Mechatronics 56 (2018) 220–241.
[11] J.L.P. Jessop, A practical primer: Raman spectroscopy for monitoring of photopolymerization systems, Polymers (2023).
[12] C.I. Higgins, T.E. Brown, J.P. Killgore, Digital light processing in a hybrid atomic force microscope: in situ, nanoscale characterization of the printing process, Addit. Manuf. 38 (2021).
[13] K. Classens, T. Hafkamp, S. Westbeek, J.J.C. Remmers, S. Weiland, Multiphysical modeling and optimal control of material properties for photopolymerization processes, Addit. Manuf. 38 (2021).
[14] M.A. Hadis, P.H. Tomlins, A.C. Shortall, W.M. Palin, Dynamic monitoring of refractive index change through photoactive resins, Dent. Mater. 26 (11) (2010) 1106–1112.
[15] G.H. Kaufmann, G.E. Galizzi, Phase measurement in temporal speckle pattern interferometry: comparison between the phase-shifting and the Fourier transform methods, Appl. Opt. 41 (34) (2002) 7254–7263.
[16] C. Meneses-Fabian, U. Rivera-Ortega, Phase-shifting interferometry by wave amplitude modulation, Opt. Lett. 36 (13) (2011) 2417–2419.
[17] K. Dorkenoo, A.J. van Wonderen, H. Bulou, M. Romeo, O. Crégut, A. Fort, Time-resolved measurement of the refractive index for photopolymerization processes, Appl. Phys. Lett. 83 (12) (2003) 2474–2476.
[18] R.E. Schwerzel, A.S. Jariwala, D.W. Rosen, A simple, inexpensive, real-time interferometric cure monitoring system for optically cured polymers, J. Appl. Polym. Sci. 129 (5) (2013) 2653–2662.
[19] X. Zhao, D.W. Rosen, Experimental validation and characterization of a real-time metrology system for photopolymerization-based stereolithographic additive manufacturing process, Int. J. Adv. Manuf. Technol. 91 (1-4) (2016) 1255–1273.
[20] X. Zhao, D.W. Rosen, Real-time interferometric monitoring and measuring of photopolymerization based stereolithographic additive manufacturing process: sensor model and algorithm, Meas. Sci. Technol. 28 (1) (2017).
[21] X. Zhao, D.W. Rosen, A data mining approach in real-time measurement for polymer additive manufacturing process with exposure controlled projection lithography, J. Manuf. Syst. 43 (2017) 271–286.
[22] X. Zhao, D.W. Rosen, An implementation of real-time feedback control of cured part height in exposure controlled projection lithography with in-situ interferometric measurement feedback, Addit. Manuf. 23 (2018) 253–263.
[23] Y. Yang, L. Li, J. Zhao, Mechanical property modeling of photosensitive liquid resin in stereolithography additive manufacturing: Bridging degree of cure with tensile strength and hardness, Mater. Des. 162 (2019) 418–428.
[24] B. Howard, N.D. Wilson, S.M. Newman, C.S. Pfeifer, J.W. Stansbury, Relationships between conversion, temperature and optical properties during composite photopolymerization, Acta Biomater. 6 (6) (2010) 2053–2059.
[25] A. Krizhevsky, I. Sutskever, G.E. Hinton, ImageNet classification with deep convolutional neural networks, Commun. ACM 60 (6) (2017) 84–90.
[26] K. He, X. Zhang, S. Ren, J. Sun, Deep residual learning for image recognition, Proc. IEEE Conf. Comput. Vis. Pattern Recognit. (2016) 770–778.
[27] A. Subasi, M. Ismail Gursoy, EEG signal classification using PCA, ICA, LDA and support vector machines, Expert Syst. Appl. 37 (12) (2010) 8659–8666.
[28] Z. Fu, V. Angeline, W. Sun, Evaluation of printing parameters on 3D extrusion printing of pluronic hydrogels and machine learning guided parameter recommendation, Int J. Bioprint 7 (4) (2021) 434.
[29] B. Zhao, M. Zhang, L. Dong, D. Wang, Design of grayscale digital light processing 3D printing block by machine learning and evolutionary algorithm, Compos. Commun. 36 (2022) 101395.
[30] L. Stanković, I. Djurović, S. Stanković, M. Simeunović, S. Djukanović, M. Daković, Instantaneous frequency in time–frequency analysis: Enhanced concepts and performance of estimation algorithms, Digit. Signal Process. 35 (2014) 1–13.
[31] F. Aloui, L. Lecamp, P. Lebaudy, F. Burel, Refractive index evolution of various commercial acrylic resins during photopolymerization, Express Polym. Lett. 12 (11) (2018) 966–971.
[32] J. de Boer, R.J. Visser, G.P. Melis, Time-resolved determination of volume shrinkage and refractive index change of thin polymer films during photopolymerization, Polymer 33 (6) (1992) 1123–1126.